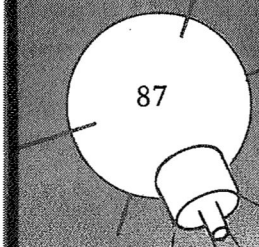

SATELLITE & MESOMETEOROLOGY
RESEARCH PROJECT

Department of the Geophysical Sciences
The University of Chicago

PATTERNS OF EQUIVALENT BLACKBODY TEMPERATURE AND REFLECTANCE OF MODEL CLOUDS COMPUTED BY CHANGING RADIOMETER'S FIELD OF VIEW

by

Jaime J. Tecson

The University of Chicago

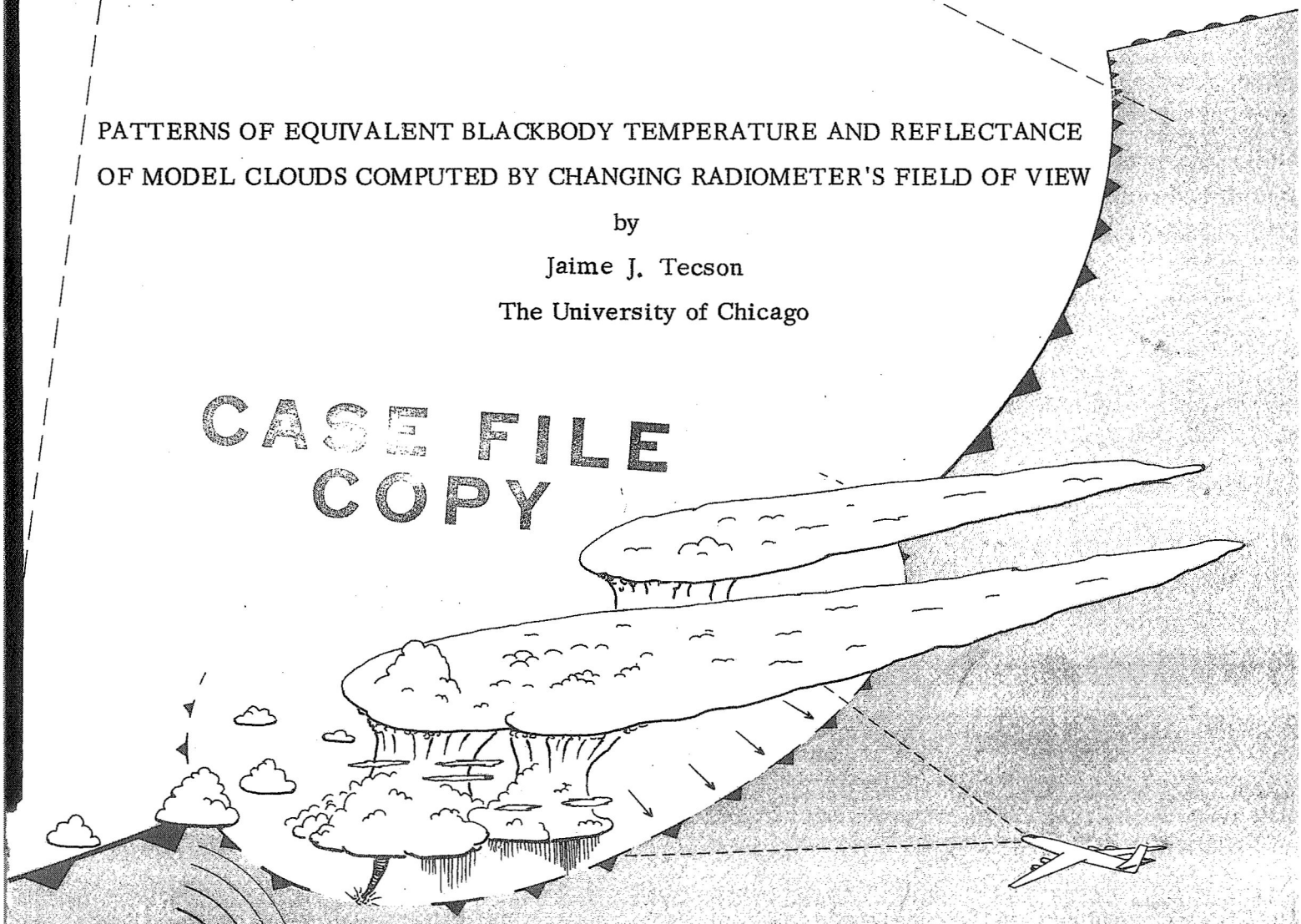

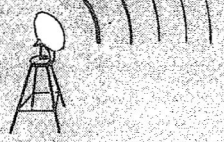

SMRP Research Paper

Number 87

May 1970

MESOMETEOROLOGY PROJECT --- RESEARCH PAPERS

1.* Report on the Chicago Tornado of March 4, 1961 - Rodger A. Brown and Tetsuya Fujita

2.* Index to the NSSP Surface Network - Tetsuya Fujita

3.* Outline of a Technique for Precise Rectif.cation of Satellite Cloud Photographs - Tetsuya Fujita

4.* Horizontal Structure of Mountain Winds - Henry A. Brown

5.* An Investigation of Developmental Processes of the Wake Depression Through Excess Pressure Analysis of Nocturnal Showers - Joseph L. Goldman

6.* Precipitation in the 1960 Flagstaff Mesometeorological Network - Kenneth A. Styber

7.** On a Method of Single- and Dual-Image Photogrammetry of Panoramic Aerial Photographs - Tetsuya Fujita

8. A Review of Researches on Analytical Mesometeorology - Tetsuya Fujita

9.* Meteorological Interpretations of Convective Nephsystems Appearing in TIROS Cloud Photographs - Tetsuya Fujita, Toshimitsu Ushijima, William A. Hass, and George T. Dellert, Jr.

10.* Study of the Development of Prefrontal Squall-Systems Using NSSP Network Data - Joseph L. Goldman

11. Analysis of Selected Aircraft Data from NSSP Operation, 1962 - Tetsuya Fujita

12. Study of a Long Condensation Trail Photographed by TIROS I - Toshimitsu Ushijima

13. A Technique for Precise Analysis of Satellite Data; Volume I - Photogrammetry (Published as MSL Report No. 14) - Tetsuya Fujita

14. Investigation of a Summer Jet Stream Using TIROS and Aerological Data - Kozo Ninomiya

15. Outline of a Theory and Examples for Precise Analysis of Satellite Radiation Data - Tetsuya Fujita

16. Preliminary Result of Analysis of the Cumulonimbus Cloud of April 21, 1961 - Tetsuya Fujita and James Arnold

17. A Technique for Precise Analysis of Satellite Photographs - Tetsuya Fujita

18.* Evaluation of Limb Darkening from TIROS III Radiation Data - S.H.H. Larsen, Tetsuya Fujita, and W.L. Fletcher

19. Synoptic Interpretation of TIROS III Measurements of Infrared Radiation - Finn Pedersen and Tetsuya Fujita

20.* TIROS III Measurements of Terrestrial Radiation and Reflected and Scattered Solar Radiation - S.H.H. Larsen, Tetsuya Fujita, and W.L. Fletcher

21. On the Low-level Structure of a Squall Line - Henry A. Brown

22.* Thunderstorms and the Low-level Jet - William D. Bonner

23.* The Mesoanalysis of an Organized Convective System - Henry A. Brown

24. Preliminary Radar and Photogrammetric Study of the Illinois Tornadoes of April 17 and 22, 1963 - Joseph L. Goldman and Tetsuya Fujita

25. Use of TIROS Pictures for Studies of the Internal Structure of Tropical Storms - Tetsuya Fujita with Rectified Pictures from TIROS I Orbit 125, R/O 128 - Toshimitsu Ushijima

26. An Experiment in the Determination of Geostrophic and Isallobaric Winds from NSSP Pressure Data - William Bonner

27. Proposed Mechanism of Hook Echo Formation - Tetsuya Fujita with a Preliminary Mesosynoptic Analysis of Tornado Cyclone Case of May 26, 1963 - Tetsuya Fujita and Robbi Stuhmer

28. The Decaying Stage of Hurricane Anna of July 1961 as Portrayed by TIROS Cloud Photographs and Infrared Radiation from the Top of the Storm - Tetsuya Fujita and James Arnold

29. A Technique for Precise Analysis of Satellite Data, Volume II - Radiation Analysis, Section 6. Fixed-Position Scanning - Tetsuya Fujita

30. Evaluation of Errors in the Graphical Rectification of Satellite Photographs - Tetsuya Fujita

31. Tables of Scan Nadir and Horizontal Angles - William D. Bonner

32. A Simplified Grid Technique for Determining Scan Lines Generated by the TIROS Scanning Radiometer - James E. Arnold

33. A Study of Cumulus Clouds over the Flagstaff Research Network with the Use of U-2 Photographs - Dorothy L. Bradbury and Tetsuya Fujita

34. The Scanning Printer and Its Application to Detailed Analysis of Satellite Radiation Data - Tetsuya Fujita

35. Synoptic Study of Cold Air Outbreak over the Mediterranean using Satellite Photographs and Radiation Data - Aasmund Rabbe and Tetsuya Fujita

36. Accurate Calibration of Doppler Winds for their use in the Computation of Mesoscale Wind Fields - Tetsuya Fujita

37. Proposed Operation of Intrumented Aircraft for Research on Moisture Fronts and Wake Depressions - Tetsuya Fujita and Dorothy L. Bradbury

38. Statistical and Kinematical Properties of the Low-level Jet Stream - William D. Bonner

39. The Illinois Tornadoes of 17 and 22 April 1963 - Joseph L. Goldman

40. Resolution of the Nimbus High Resolution Infrared Radiometer - Tetsuya Fujita and William R. Bandeen

41. On the Determination of the Exchange Coefficients in Convective Clouds - Rodger A. Brown

* Out of Print
** To be published

(Continued on back cover)

Satellite and Mesometeorology Research Project
Department of the Geophysical Sciences
The University of Chicago

PATTERNS OF EQUIVALENT BLACKBODY TEMPERATURE AND REFLECTANCE OF MODEL CLOUDS COMPUTED BY CHANGING RADIOMETER'S FIELD OF VIEW

by

Jaime J. Tecson
The University of Chicago

SMRP Research Paper No. 87
May 1970

The research reported in this paper has been supported by NASA under grant NGR-14-001-008.

PATTERNS OF EQUIVALENT BLACKBODY TEMPERATURE AND REFLECTANCE OF MODEL CLOUDS COMPUTED BY CHANGING RADIOMETER'S FIELD OF VIEW

by

Jaime J. Tecson
The University of Chicago

ABSTRACT

One of the problems encountered in determining the horizontal resolution of radiometers on board meteorological satellites used for evaluating cloud parameters from radiation data is the partial filling of the field of view by clouds. This is especially true when it becomes necessary to detect relatively small systems such as those associated with severe weather. Based on computer simulation of simplified model clouds, discussions and analyses are made of radiance and reflectance characteristics in order to find the most suitable field of view. Various scan patterns of equivalent blackbody temperature and reflectance are presented by varying the instantaneous field of view (IFOV), the width of cloud bands or diameter of circular clouds to be detected, the number of clouds, and some of their configurations.

1. Introduction

The usefulness and capabilities of meteorological satellites in detecting and following large-scale weather systems both from the research and operational points

[1]The research reported in this paper has been supported by NASA under grant NGR-14-001-008.

of view, undoubedly, have brought encouraging indications for the continuous utilization of these spacecraft for the better understanding and much-improved prediction of the weather. In the light of the various meteorological requirements that consequently arise to achieve specific purposes, certain criteria are considered in the future design of these satellites.

Detection of severe storms is an important phase in meteorological operations as well as research. Meteorological disturbances like hurricanes, tornadoes, and thunderstorms are the most destructive of this category.

Perhaps one unique characteristic of these phenomena that could be sensed by meteorological satellites is clouds overshooting from tops of cloud layers. Determining the presence of severe storms often involves separation of overshooting tops from their environment. Considering that the effective radiance of these overshooting tops is quite small, especially in the vicinity of extensive cirrus cloud shields, then this condition could well be associated with one of the more difficult cloud types to be detected by a radiometer. In this respect, if criteria could be established for an effective means of detecting such overshooting clouds, then the problem of detecting other cloud types would, comparatively, offer less difficulty, if at all.

The partial coverage by clouds of a radiometer's field of view presents one of the problems in evaluating cloud top parameters from radiation date (Fujita, 1966). The smaller the field of view of a radiometer the better chances there are, on the whole, for measuring radiation and reflectance from cloud areas. On the other hand, the effect of superimposed "noise" (Fujita and Bandeen, 1965) does play an important role in restricting the radiometer's field of view beyond certain limits.

This report attempts to present a further evaluation of the feasibility of utilizing spin scan radiometers on board geostationary meteorological satellites with emphasis on horizontal resolution for detection and identification of clouds associated with violent weather such as thunderstorms, tornadoes, hurricances, etc. In particular, this paper proposes two simplified model clouds; one, a circular cloud system overshooting from the stratified cloud tops, and the other, a cloud band system. Computer

simulation is used to provide material for the discussion of radiance and reflectance under various conditions.

2. Background

For future geostationary satellites similar to the current ATS (Applications Technology Satellites) Fujita (1970) investigated three basic design parameters; horizontal resolution, picture intervals and areas, and brightness and radiance enhancement. The report discussed, among others, a number of significant factors and their effects as a basis for determining optimum horizontal resolution contingent with meteorological requirements. Subsequently, a number of recommendations were suggested for further studies and investigations with a view to deriving additional information and other characteristics on this parameter.

This study was primarily stimulated by such recommendations.

3. The Model Clouds and Assumptions

Two simplified model clouds are presented. One involves a circular overshooting cloud top system for radiance approximations and another a cloud band system for reflectance computations.

3.1 Circular Overshooting Cloud

The overshooting clouds from the tops of a broad cirrus base occur commonly among severe storm-producing systems such as thunderstorms. As a first step in evaluating parameters for determining a meaningful field of view for a spin scan infrared radiometer, this overshooting cloud system is established as a model.

It is assumed that this cloud or system of clouds protrudes as a dome from a broad cirrus cloud base at approximately 13 kms with the cloud top shooting upward by about 2 kms (see Fig. 1). This environmental cirrus is assumed to have an emissivity of 100%. As viewed downwards, the horizontal plane is circular in shape. The dome has a cross-section the shape of a half-ellipse with the major axis as its base.

The diameter of the base is variable.

Using a mean tropical atmosphere sounding (Riehl, 1954), the temperature at the base and the surrounding cirrus is assigned as 213°K (-60° C) while at the top it is 201°K (-72°C). The relation between temperature change and height is taken to be linear. Since the detection of overshooting cloud tops requires a comparatively narrow field of view, beam radiation or radiance toward the satellite radiometer would be directed mostly along the optical axis (NASA, 1965). For this experimental purpose, therefore, the relationship between equivalent blackbody temperature and effective radiance for Nimbus III HRIR Flight Unit F-5 (NASA, 1969) is used as a reasonably good approximation.

3.2 Cloud Bands

A simplified model is proposed consisting essentially of cloud bands of varying widths. The lengths of these bands are aligned perpendicular to the direction of scan by the radiometer and are assumed infinite. The reflectance of the individual elements within the cloud is assumed to be 100% while outside values are nil.

4. Simulation Procedures

Computer simulations using these models were run through the IBM 7094 computer facility of the University of Chicago.

4.1 Effective Radiance, Spectral and Spatial Responses of a Radiometer

A radiometer is characterized by spectral response, ϕ_λ, and spatial response, ϕ_ω, that filter the radiant energy being sensed by it. The total power received by the radiometer (Fujita and Grandoso, 1967) can be written as

$$p = A \iint N_{(\lambda,\omega)}\, \phi_\lambda\, \phi_\omega\, d\omega\, d\lambda \qquad (1)$$

where A denotes the area of the lens; $N_{(\lambda,\omega)}$, the spectral radiance reaching the sensor given as a function of λ and ω; ϕ_λ, the spectral response; ϕ_ω, the

spatial response; and $d\omega$, the element of solid angle as viewed from the satellite. Within reasonable accuracy, we may approximate both responses by those given in the Nimbus III User's Guide (NASA, 1969). The spectral response, ϕ_λ ,is the combined effect of reflectivity and transmittance calculated from laboratory measurements of the optical components of the radiometer system. The spatial response, ϕ_ω , is the effect on the incoming radiant energy as focused on various sections of the detection surface. Adopting NASA's pre-flight calibration of the radiometer under laboratory conditions (with the use of a blackbody target where N_λ does not vary with ω), the right side of Eq. (1) can be reduced to

$$p = A\int N_\lambda \phi_\lambda d\lambda \int \phi_\omega d\omega = A\bar{\bar{N}}\int \phi_\omega d\omega \qquad (2)$$

where $\bar{\bar{N}} = \int N_\lambda \phi_\lambda d\lambda$.

The quantity $\bar{\bar{N}}$ is called the effective radiance and represents the integrated radiance detected by the radiometer's sensor within its spectral response. Combining Eqs. (1) and (2), we obtain

$$A\iint N_{(\lambda,\omega)} \phi_\lambda \phi_\omega \, d\omega d\lambda = \bar{\bar{N}} A \int \phi_\omega d\omega . \qquad (3)$$

Then,
$$\bar{\bar{N}} = \frac{\iint N_{(\lambda,\omega)} \phi_\lambda \phi_\omega \, d\omega d\lambda}{\int \phi_\omega d\omega}$$

$$= \frac{\int \bar{N}_\omega \phi_\omega d\omega}{\int \phi_\omega d\omega} \qquad (4)$$

where $\bar{N}_\omega = \int N_{(\lambda,\omega)} \phi_\lambda d\lambda$ is the elemental effective radiance within the radiometer's field of view.

For computer simulation purposes, Eq.(4) is approximated in discrete form as

$$\bar{\bar{N}} = \frac{\sum\sum \bar{N}_{(x,y)} \phi_{(x,y)} \Delta x \Delta y}{\sum\sum \phi_{(x,y)} \Delta x \Delta y} \qquad (5)$$

where again $\bar{N}_{(x,y)}$ is the elemental effective radiance within the radiometer's field of view,

and $\phi_{(x,y)}$ is the spatial response.

4.2 Reflectance

The study of reflectance characteristics due to the partial coverage of clouds within the radiometer's field of view is carried out through a similar simulation process using the general form of Eq. (5) and is written as

$$\bar{R} = \frac{\sum\sum R_{(x,y)} \phi_{(x,y)} \Delta x \Delta y}{\sum\sum \phi_{(x,y)} \Delta x \Delta y} \qquad (6)$$

where $\bar{R}$ is defined as the measured reflectance integrated by the radiometer's sensor and $R_{(x,y)}$ the elemental reflectance of the individual element within the cloud.

4.3 Design of Grid, Input and Output Values

A rectangular mesh is used with equal distances between grid points. For radiance computations, circles of various diameters to simulate clouds are drawn with sufficient separation between them to insure that computed values for one cloud area are unaffected by the adjoining ones. For each grid point within a circle, a normalized effective radiance value (in watts per square meter per steradian) is assigned in relation to its height such that the center value, which corresponds to the top of the dome, is always the coldest spot. For each grid point outside the circle, which is considered as the environment, a fixed normalized value for effective radiance is also assigned. This corresponds to the cloud base equivalent blackbody temperature.

For reflectance evaluations, vertical strips of various widths representing cloud bands are likewise drawn on the grid. For each grid point within a strip, a reflectance value of 100% is assigned. For those points outside the strip, a zero percent reflectance value is set. Of course, a multitude of cloud band configurations can be simulated; they can be handled as input changes and may not require program changes.

The program was designed such that it would simulate a series of passes by a

hypothetical circular-shaped field of view over the whole length and breadth of the grid; decidedly a more efficient approach than running individual programs for each cloud configuration. In the output format, at each and every grid point location is indicated whatever integrated effective radiance or measured reflectance values the radiometer senses, assuming that the center of field of view is located at this grid point and the system is viewing vertically downward. The field of view is fixed in diameter with respect to the grid size and always remains within the grid boundaries as it scans.

The spatial response of the radiometer is approximated from the 10 to 11 micron channel angular field of view of the Nimbus III User's Guide (see Fig. 2). The Instantaneous Field of View (IFOV) or half-power scan diameter ($\phi_{1/2}$) is two-thirds of the maximum power scan diameter (ϕ_m).

Analyses of isotherms (equivalent blackbody temperatures) and reflectance are performed manually on square grid scale from computer output values in order to preserve dimensions of all patterns for comparison purposes.

5. Analyses and Discussion

A radiometer measures essentially beam radiation within an angular field of view conventionally referred to as the IFOV, which, at a given altitude, corresponds to a subsatellite ground resolution at the nadir.

In view of the importance of the early detection of small cells of severe storms in the initial stages of development, small IFOV's are ideal. In the visible range of the electro-magnetic spectrum, Fujita (1970) has recommended a 0.10 milliradian (mr) or 2 nautical mile (n.m.) IFOV for cloud detection of convective cells. For detection in the infrared region, a 0.25 mr or 5 n.m. IFOV, however, is proposed, thereby giving sufficient allowance for discriminating noise interference which might show up in the radiometer system.

5.1 Radiance

It might be interesting to note some characteristic configurations or patterns that might appear when single circular clouds are scanned by radiometers of different

instantaneous fields of view. Figure 3 shows one such pattern when four individual clouds of different diameters and their immediate surroundings are scanned by an IFOV of 0.10 mr, while Figure 4 exhibits other patterns as the same four clouds are scanned by a 0.27 mr or 5.33 n.m. IFOV. To make these sets of figures readily comparable, the sizes of the corresponding clouds, shown as stippled areas in both diagrams, are reduced to the same scale. These patterns result when the radiometer, viewing vertically downward, makes a series of passes and completely scans an isolated overshooting cloud and its surrounding cirrus base one at a time.

Analysis is made of the integrated effective radiance values, $\bar{\bar{N}}$, which are converted to equivalent blackbody temperatures, T_{BB}. As could be observed from the upper portions of the figures, the T_{BB}'s are concentric about each cloud center. Since the larger IFOV integrates values over a bigger area, much of the surrounding cirrus is scanned with each cloud, especially those with smaller cloud diameters. Consequently, the resulting integrated effective radiance values tend to give correspondingly higher temperature readings than are to be expected and, therefore, fail to portray the "true" picture of the temperature characteristic of each cloud scanned. This conclusion becomes evident from the lower portions of the figures where two sets of overlapping curves are drawn to indicate the temperature profile corresponding to each point of the cloud on the upper portion being scanned. For each cloud, the shallow curve represents the temperature response of the radiometer as it scans across the overshooting cloud and surroundings through its center, as, for example, from left to right. The deep curve, which is in the background, indicates the "ideal" temperature pattern of the cloud; that is, when it is scanned in the same manner by the radiometer with a theoretically zero IFOV. From these comparisons it may be generally remarked that the larger the IFOV and the smaller the cloud, the lesser the degree to which the radiometer response approximates the "true" temperature pattern.

Figure 5 shows the curves for the two IFOV's in Figures 3 and 4 drawn with the cloud diameter, D, vs. detection efficiency, $\bar{N}_e - \bar{\bar{N}}_c / (\bar{N}_e - \bar{N}_c)$, as coordinates. The detection efficiency is thus defined by the above ratio where $\bar{N}_e$ is the elemental effective

radiance of the environmental cirrus cloud base; $\bar{N}_c$, the elemental effective radiance at the center of the single circular overshooting cloud top; and $\bar{\bar{N}}_c$, the integrated effective radiance at the center of the same cloud top. Taking into account the effect of the noise equivalent temperature difference, $NE\Delta T$, from data given by Alishouse at 200°K and 100 rpm spacecraft rotation, detection of individual clouds by a 0.27 mr IFOV for the infrared sensing radiometer becomes possible only when the diameters are at least three miles. Especially for the 0.27 IFOV curve, this diagram might suggest the feasibility of estimating with some reliability the diameters of single circular clouds from detection efficiencies, particularly in the 3-to 8-mile cloud diameter range. The vertical scales to the right of the figure shows the $\bar{N}_e - \bar{\bar{N}}_c$ readings (normalized values) alongside the ΔT scale which corresponds to the temperature equivalent in degre es C of the effective radiance measurements $\bar{N}_e - \bar{\bar{N}}_c$.

Some aspects and configurations in multi-cloud systems of overshooting cloud tops might also be worth noting. When a circular overshooting cloud exists near another, or when several clouds are grouped in a cluster, and are scanned by a radiometer, a certain degree of interaction takes place between them and the surrounding areas when they are certain distances apart.

Patterns of measured temperatures for twin circular clouds each of 4-mile diameter as scanned by an IFOV of 0.27 mr tracing a path across the clouds centers are shown in Figure 6. Again, stippled circles indicate the top view of the clouds in the various stages of separation. Surrounding them are closed isotherms or T_{BB} (equivalent blackbody temperature) lines. Analysis is performed after superimposing individual cloud patterns from the output format in accordance with the configuration desired and adding corresponding grid point values. When clouds are close together (edge-to-edge), isotherms do not betray the existence of two distinct cloud tops but rather indicate a form somewhat similar to an elliptical mound. As the clouds are separated farther, the isotherms tend to become concentric around each cloud until a point is reached at which each cloud attains the characteristics of a single four-mile diameter circular cloud as represented in Figure 4. Below each isotherm pattern in Figure 6 are

drawn the respective temperature profiles, the shallow curve represents the radiometer response curve while the other curve indicates a theoretically zero IFOV scan profile as the radiometer makes a pass across the center of the twin clouds. As is suggested by this figure, one direct method of estimating the degree of separation between twin clouds is to determine twin cloud ΔN or $TC\Delta N$ defined as

$$TC\Delta N = \bar{\bar{N}}_C - \bar{\bar{N}}_M \tag{7}$$

where $\bar{\bar{N}}_C$ is the integrated effective radiance at the cloud center and $\bar{\bar{N}}_M$ is the integrated effective radiance at the midpoint between the clouds. The lower portion of Fig. 7 shows the curves for $\bar{\bar{N}}_C$ and $\bar{\bar{N}}_M$ for non-normalized values. The upper portion represents $TC\Delta N$ where positive values indicate that no separation is possible while negative values indicate that detection of separation becomes apparent. Theoretically, this would occur when the clouds are at least one mile apart; that is, not considering the effect of $NE\Delta T$. If such is considered and since the relation between effective radiance and equivalent blackbody temperature has been established for this model, individual clouds should be separated no less than three miles apart in order that they can be individually detected. The magnitude of $TC\Delta N$ roughly indicates the distance of separation between these clouds. Beyond six miles separation, the twin clouds are detected as single circular clouds.

Figures 8 and 9 show the isotherm (T_{BB}) patterns of three and four circular cloud clusters, respectively. Each cloud is shown stippled and has a diameter of four miles. These multi-cloud clusters are scanned by a 0.27 mr IFOV. Analyses are accomplished by the method of graphical addition (Saucier, 1955) of the integrated effective radiance of each individual cloud and later converted to equivalent blackbody temperatures. In both figures, three configurations are shown, when they are closest together without cloud overlap (edge-to-edge), when each cloud is two miles away from the nearest one, and finally when four miles away from the nearest one. It is noticeable that multi-cloud clusters brought together edge-to-edge exhibit concentric isotherm patterns similar to that of a single circular cloud but of different configurations. Again,

as the clouds become separated beyond six miles, the patterns become those of individual circular clouds.

(For the basic concepts and more relevant discussion on radiance as it pertains to horizontal resolution, refer to SMRP Report No. 84 by Fujita (1970)).

5.2 Reflectance

The effects of the partial filling of the radiometer's field of view on cloud reflectance characteristics should also be understood and appreciated to derive more meaningful interpretation of satellite radiation data. To a large extent, the behavior is similar to that which influences radiance.

When a one-mile-wide cloud band is scanned by a radiometer with different fields of view, the relative sizes of the reflectance patterns are shown on the upper portion of Fig. 10. The stippled areas indicate the cloud bands, each one mile wide, and drawn to the same scale. The arching solid and dashed lines are isolines of reflectance values in percent (%) as analyzed from the output values. It is recalled that these values result as the radiometer scans the cloud band and its surroundings in a series of passes. Inserted between the reflectance lines of the 13.33 n.m. IFOV scan pattern are two similarly shaped reflectance patterns for the smaller IFOV's. This is resorted to for purposes of comparison only and necessitated by limitations in space.

Since the larger IFOV integrates values over a bigger area with a given cloud much of the surrounding area is scanned with each cloud. This effect is shown in the lower portion of the figure which represents the reflectance profiles of the cloud as it is progressively scanned by a radiometer making a pass across and through the middle of an infinitely long cloud band shown above. Below each reflectance pattern are two sets of lines, a curve and a rectangular-shaped line. The smooth curve indicates the reflectance response of the radiometer as it cuts through the surrounding areas and across the cloud, the vertical bar fine-line depicts the reflectance of the cloud when similarly scanned this time by a theoretically zero IFOV. Comparison of the curves show that smaller IFOV's tend to approximate better the "true" or ideal reflectance patterns of these cloud bands since the field of view gets to be more filled

with clouds. In this respect, the measured reflectance varies only with the ratio of the instantaneous field of view over the width of the cloud (IFOV/W).

Figure 11 shows the maximum measured reflectance obtainable for single cloud bands of varying IFOV/W. 100% measured reflectance is attained when IFOV/W is at most 0.67; that is, when the cloud band covers entirely the field of view.

If it is desired, however, to find out the maximum percentage reflectance as measured by different IFOV's on various widths of cloud bands, Fig. 12 would show such relationship. For example, a 100% response on a 6-mile-wide cloud is achieved by an IFOV of at most 4 n.m. or a 0.10 mr IFOV would register about 57%, 94%, and 100% measured reflectance values for, respectively, a one-mile, two-mile, and three-mile-wide cloud band being scanned.

When two cloud bands, each one mile wide, are placed with various distances between them and scanned by a radiometer with an IFOV of, say, 1.67 n.m., the reflectance characteristics are those that appear in Fig. 13. As before, the stippled areas represent the cloud bands about which are drawn isolines of reflectance as these twin cloud bands and surrounding area are scanned by a series of passes of the radiometer. The lower portion shows the reflectance profile during one pass of the radiometer across and through the middle of an infinitely long twin-cloud band. The smooth curve indicates the measured reflectance integrated by the radiometer's sensor, the vertical bar thin-line depicting measured reflectance integrated by a theoretically zero IFOV.

A glance at the profiles of the two patterns would indicate that similar to radiance analysis, one method of detecting the existence of the bands could be achieved by defining twin cloud band ΔR or $TB\Delta R$ as

$$TB\Delta R = \bar{R}_c - \bar{R}_m \tag{8}$$

where $\bar{R}_c$ is the measured reflectance integrated by the radiometer's sensor at the center of either cloud band and $\bar{R}_m$ is the measured reflectance integrated by the radiometer's

sensor at the midpoint between the two bands.

It should be noted that the one-mile-wide cloud band example in Figs. 10 and 13 were chosen purely for simplicity purposes. Since IFOV/W is a constant, then if it is desired instead to simulate a pattern for 4-mile-wide cloud bands, the configuration in Fig. 13 would remain the same if it were scanned by an IFOV of about 6.67 n.m.

Fig. 14 shows the relationship between S/IFOV and IFOV/W. Isolines are $TB\Delta R$ values in percent (%). Negative values would depict single "hump" appearance in the profile while positive values would indicate a measure of the degree of separation between the cloud bands by the presence of two "humps". At points near the origin the degree of reliability becomes less and values exceeding 100% are not encountered.

As a consequence of Fig. 14, it becomes possible to determine the minimum distances that various twin-clouds should be separated in order to detect them as individual clouds when scanned by different IFOV's (see Fig. 15). If an IFOV of 0.10 mr is used, then for a radiometer response that could indicate these clouds as individual bands, the separation between them should be at least three-fourths of a mile. At less than that distance, only one hump will show up. Furthermore, any twin cloud of more than three miles width can be detected as two clouds at the slightest distance they are brought apart for this particular IFOV.

Referring back to the example of the twin one-mile-wide cloud bands, it might be interesting to find out the behavior of the $TB\Delta R$'s for different IFOV's (see Fig. 16). This shows that the larger the IFOV, the farther the distance that is required to detect, and faintly at that, individual cloud bands (by following the 0% line). It can be seen that for an IFOV of 0.10 mr, $TB\Delta R$ would not exceed 60% no matter how far the twin clouds are separated. $TB\Delta R$ values will not exceed 100%.

Finally, the upper portion of Fig. 17 illustrates a $TB\Delta R$ curve for twin clouds, each a mile wide as scanned by a radiometer with an IFOV of 1.67 n.m. Correspondingly, at the lower portion are plotted the curves $\bar{R}_c$ and $\bar{R}_m$ showing the relation $TB\Delta R = \bar{R}_c - \bar{R}_m$. Negative values of $TB\Delta R$ indicate that no separation is possible. Detection of separation is noticed when $TB\Delta R$ is positive and this occurs when the cloud bands are at least one-half mile apart. The magnitude of $TB\Delta R$ would also indicate the distance of

separation between these cloud bands.

6. Conclusions

Based on the simplified models assumed in this report, it is found that smaller IFOV's can more readily and quite reliably detect cloud cells within the three-to-eight mile diameter range. However, the limitations imposed by the $NE\Delta T$ have necessitated enlarging the radiometer field of view somewhat. Contingent with desired meteorological requirements to detect relatively small-magnitude clouds on board future geostationary meteorological satellites, a 0.10 mr (or 2.0 n.m.) IFOV for the visible range and another in the order of 0.25 mr (or 5 n.m.) IFOV for the infrared range appear reasonable.

Analyses of equivalent blackbody temperatures on overshooting single or multiple circular cloud tops and reflectance on cloud bands have revealed basic and distinctive scan patterns. It is noticeable that a single pattern of concentric isotherms will result regardless as to whether the cloud is singular or a four-cluster system provided they are drawn very close together. A criteria for determining limits of distances in order to detect separation for twin clouds are presented; however, none has been attempted for the three-or four-cloud systems.

Variations in the model clouds may be accomplished with minor changes in the computer program.

REFERENCES

Fujita, T. T., 1966: Results of the computation of cloud heights, emissivity, and cover from long-and short-wave radiation data. Proceedings of the XVII Congress of International Astronautical Federation, Madrid, October 1966, 155-162.

_____, 1970: Basic problems on cloud identification related to design of SMS-GOES spin scan radiometers. SMRP Research Paper No. 84, The University of Chicago.

_____, and W. Bandeen, 1965: Resolution of the nimbus high resolution infrared radiometer. SMRP Research Paper No. 40, The University of Chicago.

_____, and H. Grandoso, 1967: A proposed method of estimating cloud-top temperature, cloud covers, emissivity and cloudiness from short-and long-wave radiation data obtained by medium-resolution scanning radiometers. SMRP Research Paper No. 48, The University of Chicago.

NASA, 1965: Nimbus I high resolution radiation data catalog and user's manual, Vol. I. Goddard Space Flight Center, Greenbelt, Maryland, 226 pp.

_____, 1969: The Nimbus III user's guide. Goddard Space Flight Center, Greenbelt, Maryland, 238 pp.

Riehl, H., 1954: Tropical Meteorology. McGraw-Hill Book Co., New York, 392 pp.

Saucier, W. J., 1955: Principles of Meteorological Analysis. The University of Chicago Press, Chicago, 438 pp.

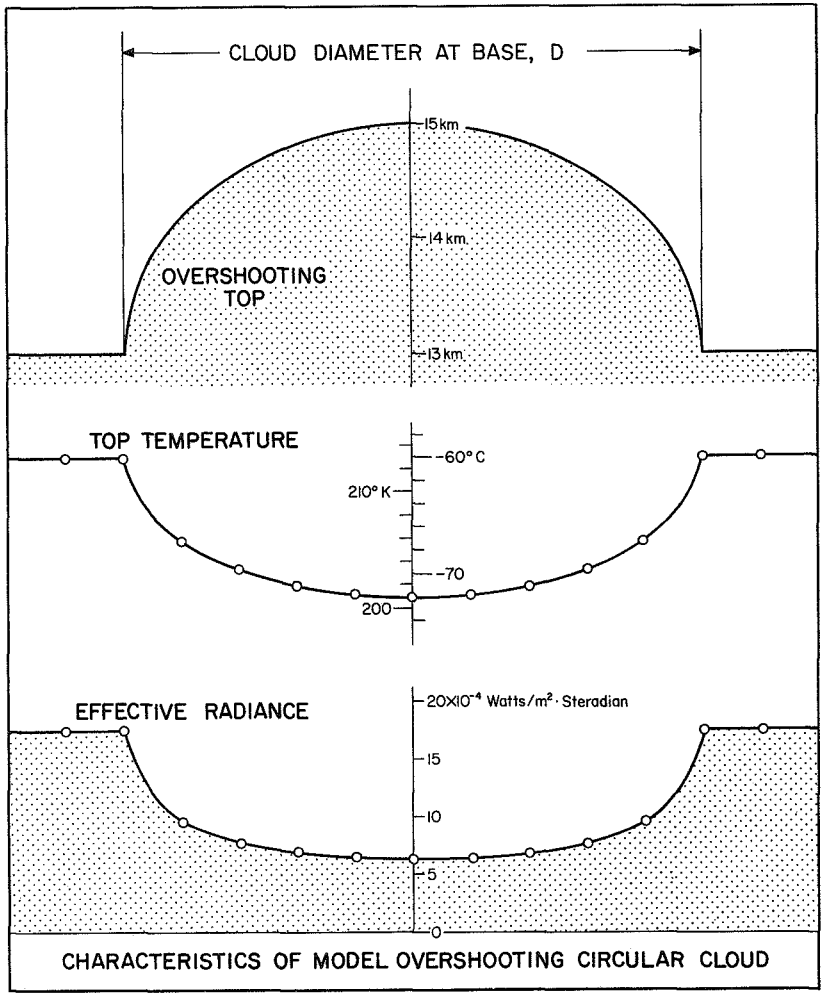

Fig. 1. Relationship between height, equivalent blackbody temperature and effective radiance in a simplified model cloud with overshooting top. (From Fujita, SMRP No. 84, Basic Problems on Cloud Identification Related to the Design of SMS-GOES Spin Scan Radiometers)

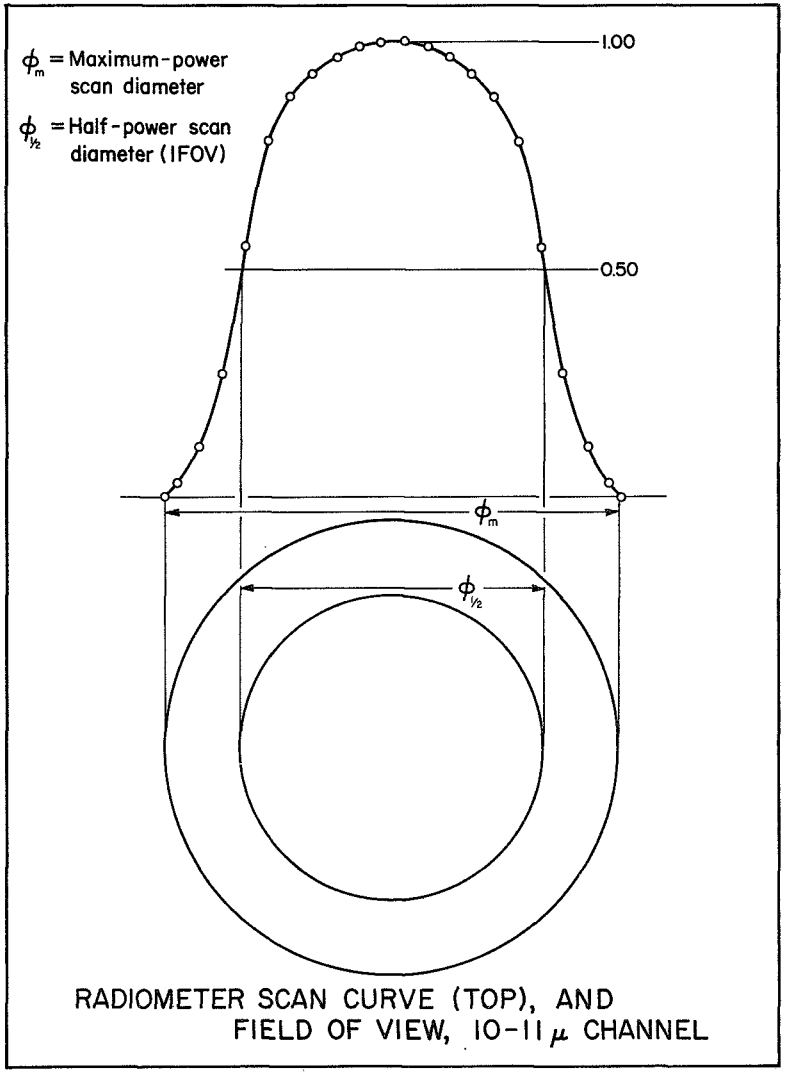

Fig. 2. Spatial response radiometer curve (upper portion) and field of view (lower portion) used in the simulation program for the circular overshooting cloud model.

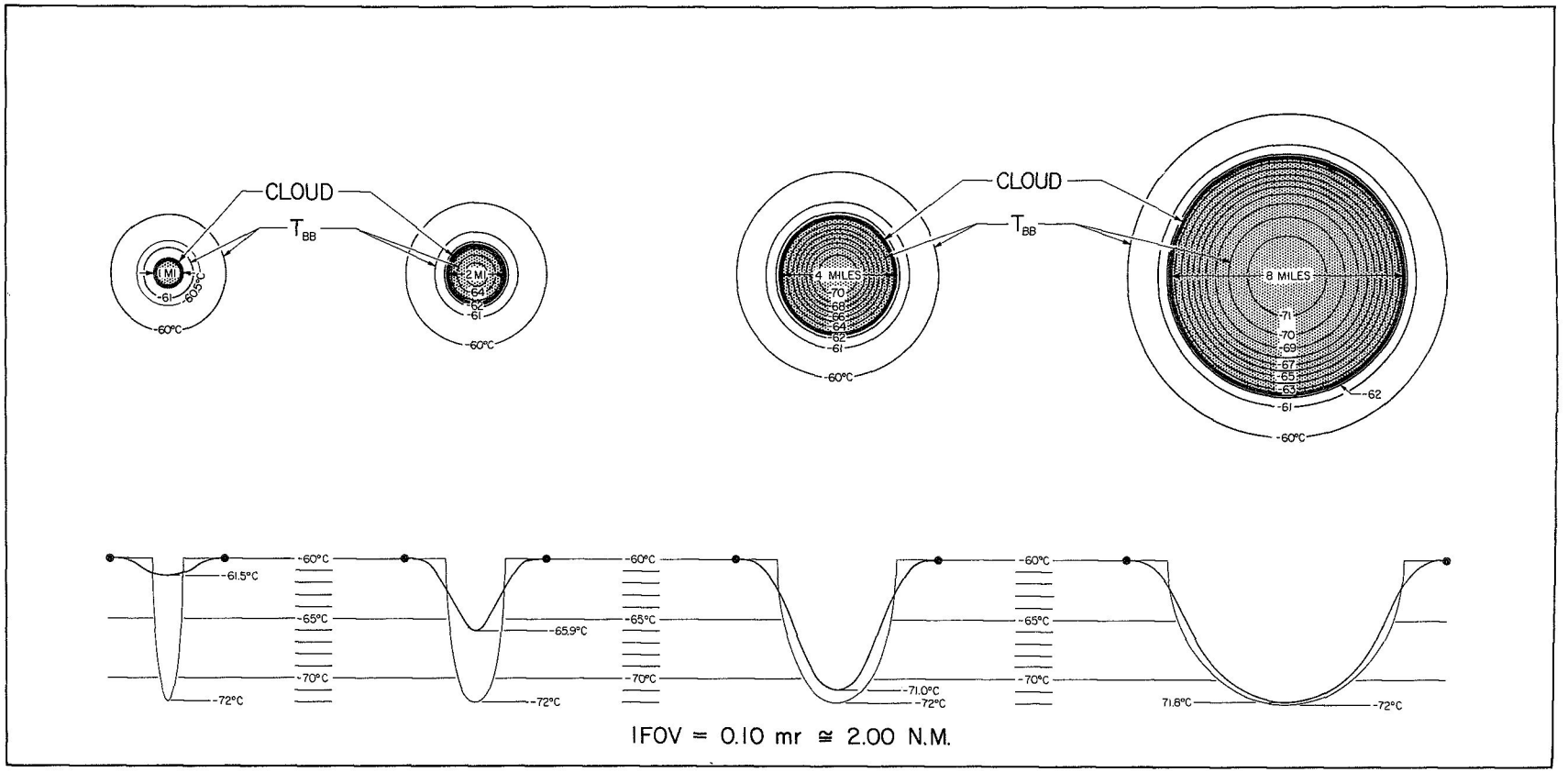

Fig. 3. Simulated patterns of equivalent blackbody temperature or T_{BB} (upper portion) relative to various sizes of single circular clouds and corresponding profiles (lower portion) when scanned by a 0.10 mr IFOV radiometer. The shallow curves represent computed temperatures while the deep curves indicate response from theoretically zero IFOV. The stippled areas denote clouds of various diameters.

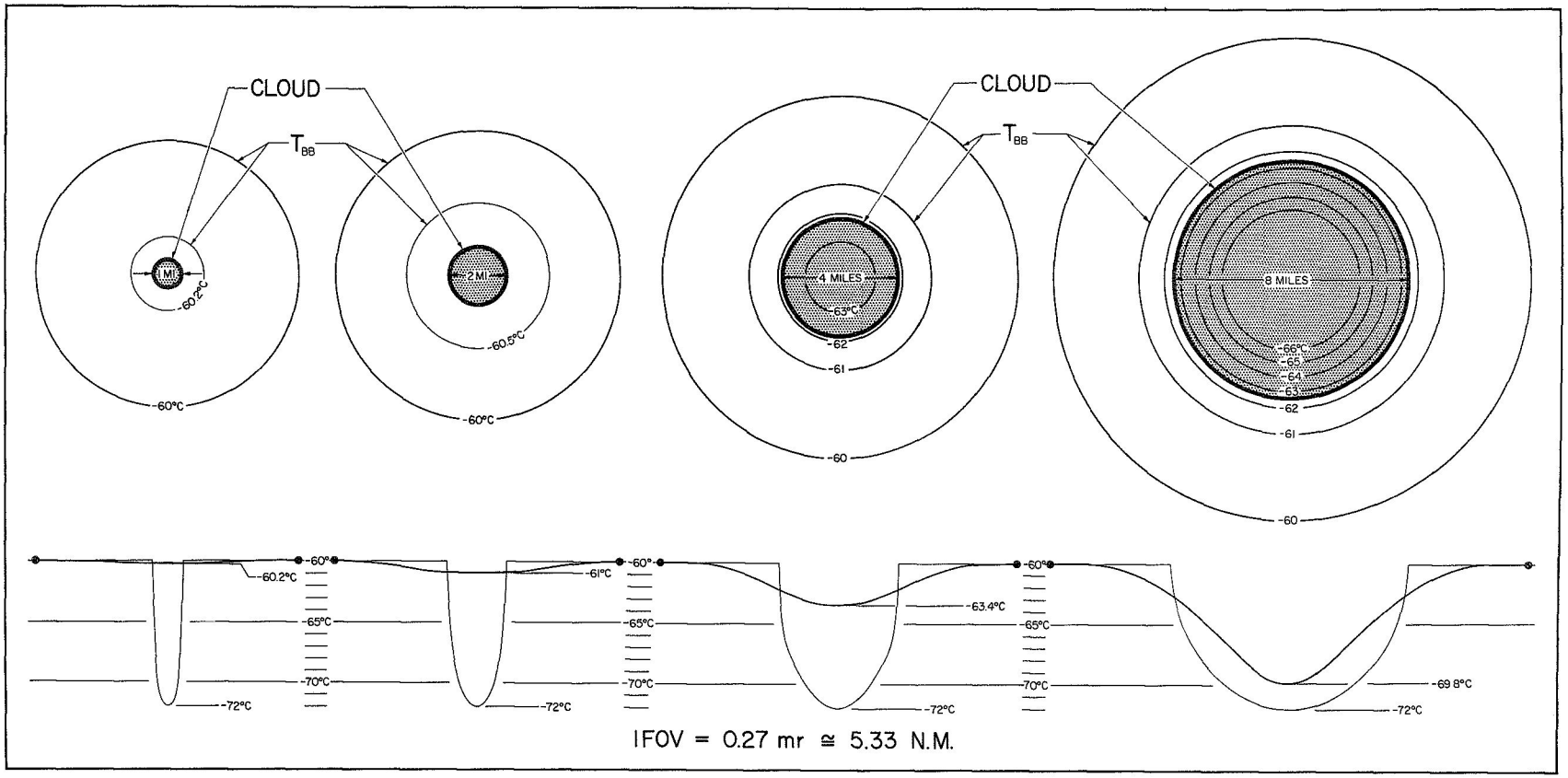

Fig. 4. Simulated patterns of equivalent blackbody temperature or T_{BB} (upper portion) relative to various sizes of single circular clouds and corresponding profiles (lower portion) when scanned by a 0.27 mr IFOV radiometer. The shallow curves represent computed temperatures while the deep curves indicate response from theoretically zero IFOV. The stippled areas denote clouds of various diameters.

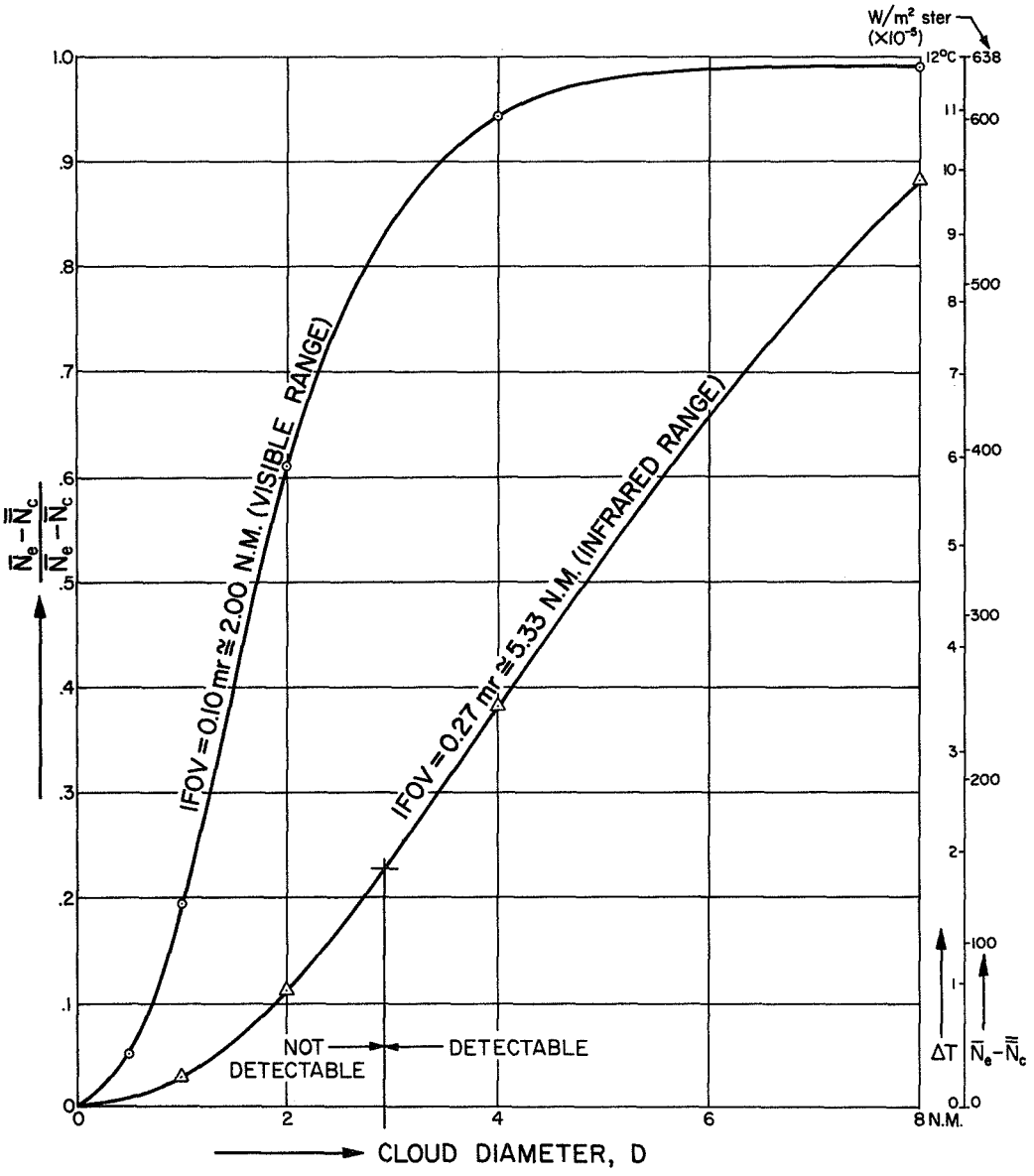

Fig. 5. Detection efficiency of radiance of single circular clouds for different IFOVs. Detectable limit for 0.27 mr IFOV due to NEΔT is shown. Radiance values are normalized. $\bar{N}_e$ is the elemental effective radiance of the environmental cirrus base; $\bar{N}_c$, the elemental effective radiance at the center of the cloud top; and $\bar{\bar{N}}_c$, the integrated effective radiance at the center of the same top.

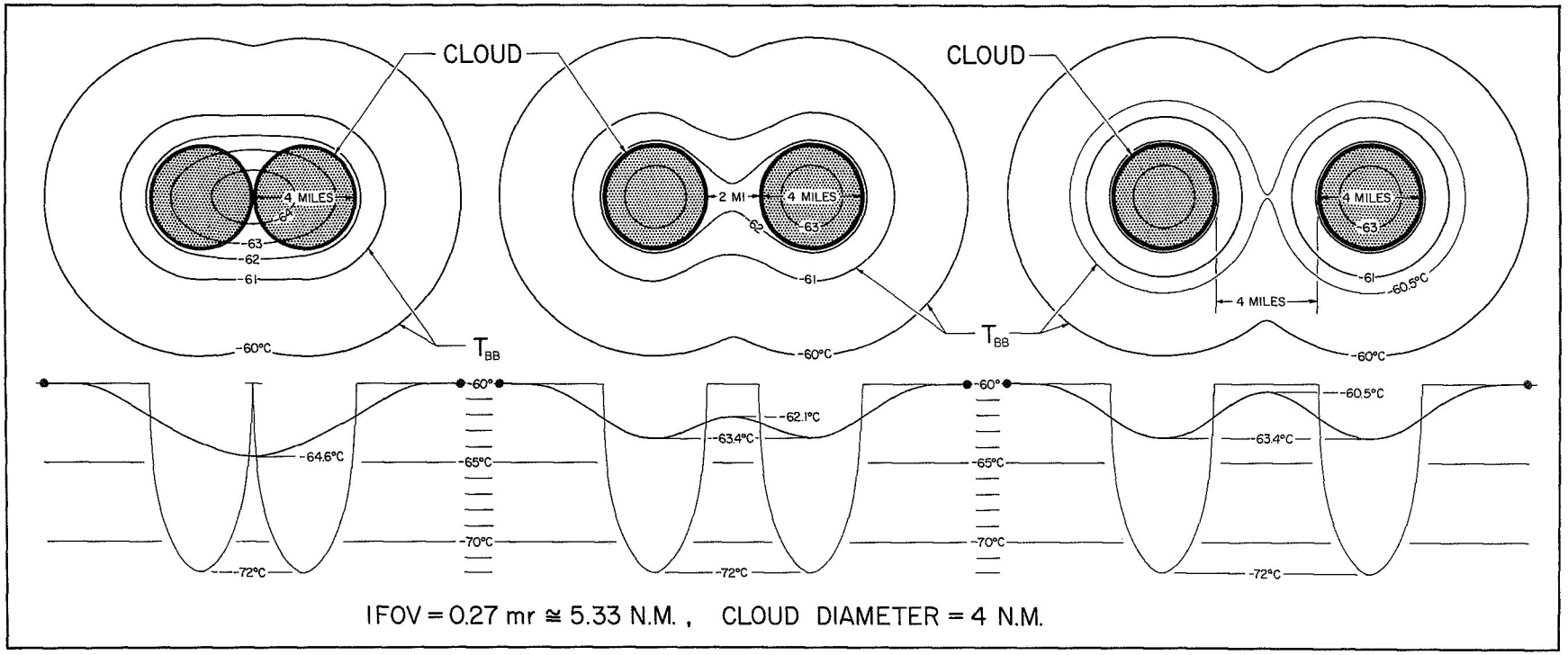

Fig. 6. Simulated patterns of equivalent blackbody temperature or T_{BB} (upper portion) relative to various distances separating twin 4-mile diameter circular clouds and corresponding profiles (lower portion) when scanned by a 0.27 mr IFOV radiometer. The shallow curves represent computed temperatures while the deep curves indicate response for theoretically zero IFOV. The stippled areas denote the twin 4-mile diameter clouds.

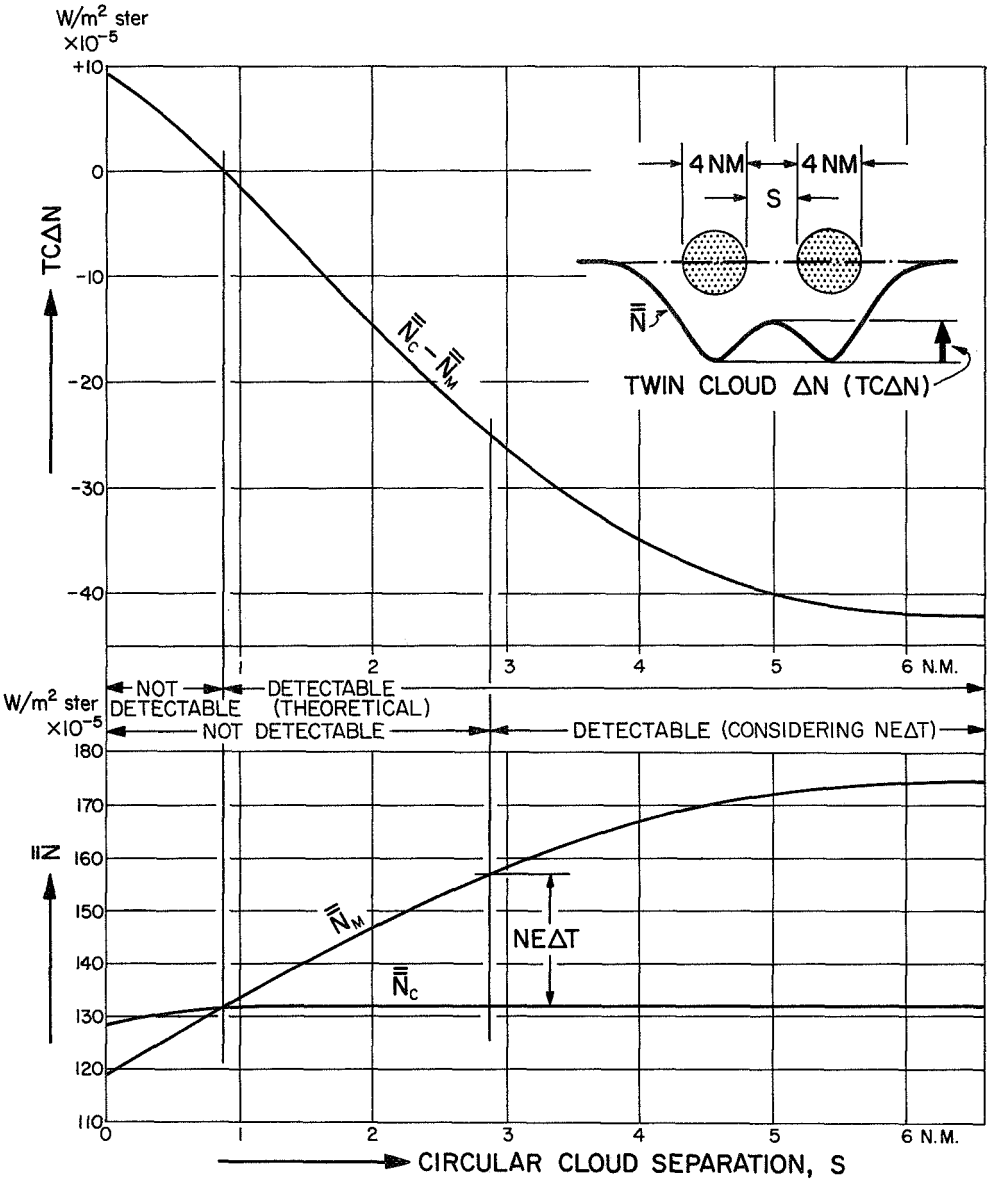

Fig. 7. Non-normalized effective radiance curves (lower portion) for twin circular clouds of 4-miles diameter at various distances apart when scanned by a 0.27 mr IFOV. $\bar{\bar{N}}_C$ is the integrated effective radiance at the cloud center and $\bar{\bar{N}}_M$ is the integrated effective radiance at the midpoint between clouds. Limits for detecting presence of two clouds are indicated with and without considering NEΔT. Upper part shows curve for $\bar{\bar{N}}_C - \bar{\bar{N}}_M$.

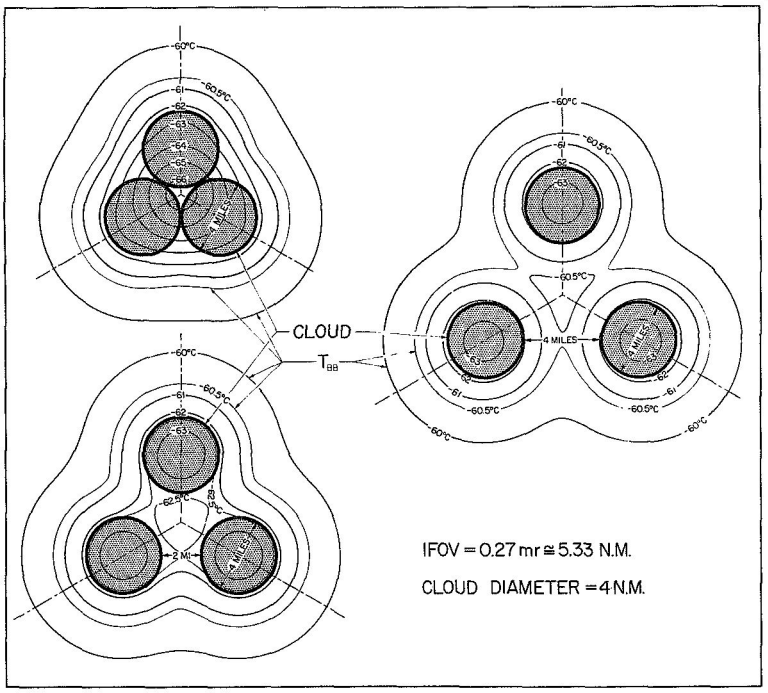

Fig. 8. Simulated patterns of equivalent blackbody temperature or T_{BB} relative to various distances apart of clouds in a three-cloud-cluster when scanned by a 0.27 mr IFOV. The stippled areas represent the circular clouds each 4 miles in diameter and the distances between clouds are assumed identical.

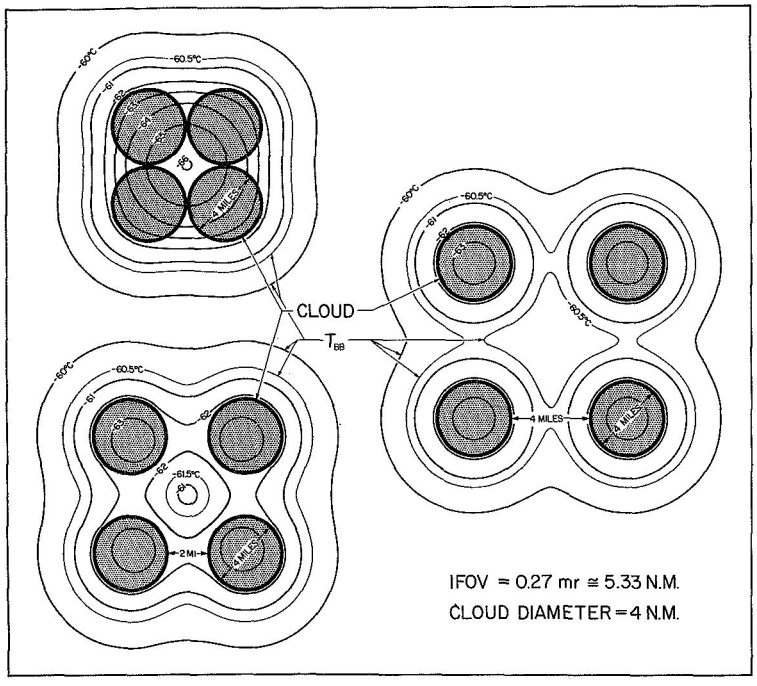

Fig. 9. Simulated patterns of equivalent blackbody temperature or T_{BB} relative to various distances apart of clouds in a four-cloud-cluster when scanned by a 0.27 mr IFOV. The stippled areas represent the circular clouds each 4 miles in diameter and the distances between clouds are assumed identical.

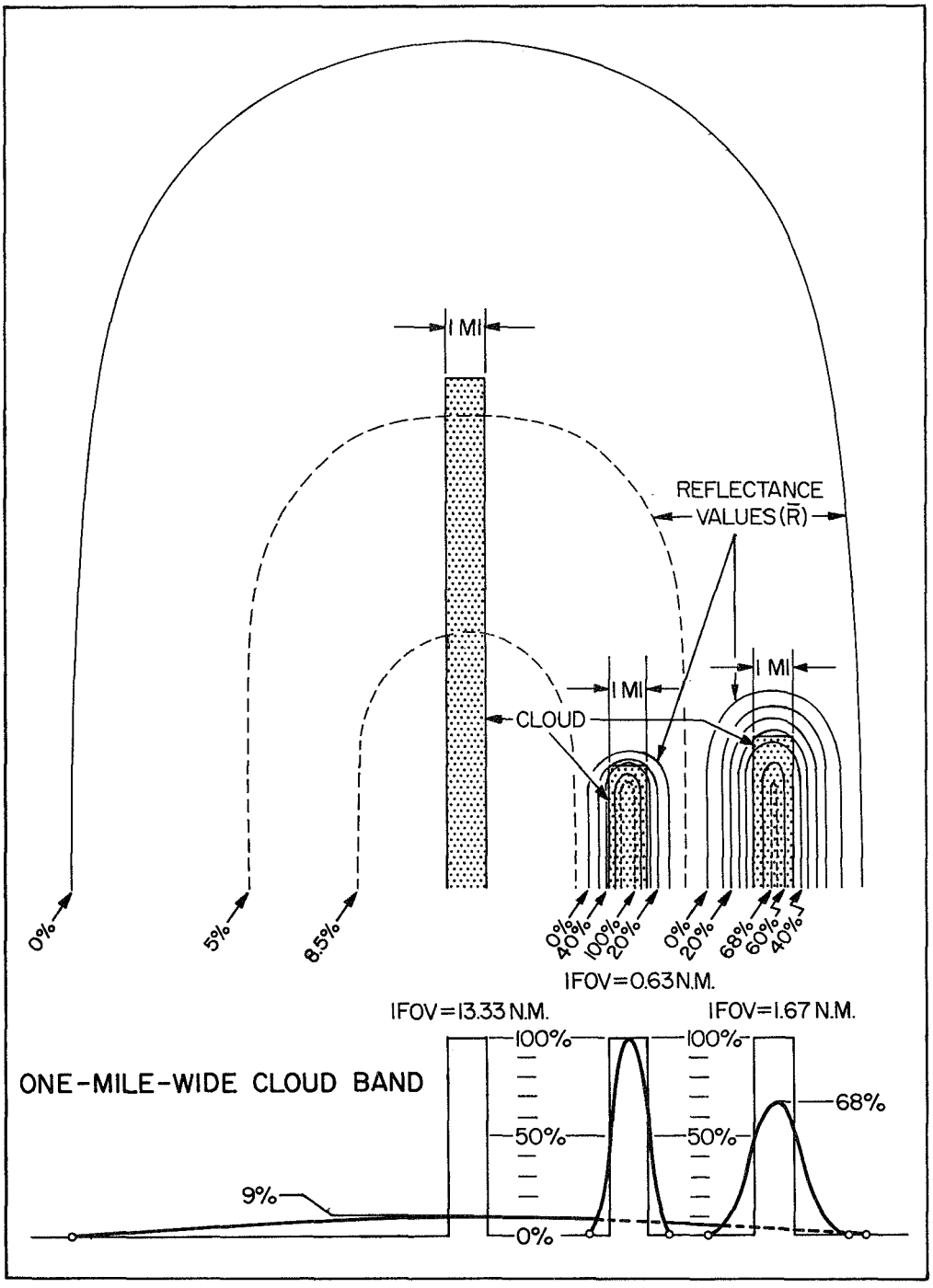

Fig. 10. Simulated patterns of reflectance values (upper portion) relative to a single cloud band of infinite length and corresponding profiles (lower portion) when scanned by different IFOVs. The curves in the lower portion represent computed reflectance for the particular IFOV while the vertical bar areas indicate response from theoretically zero IFOV. The patterns are superimposed for comparison only. The stippled areas denote cloud bands uniform ly one mile wide.

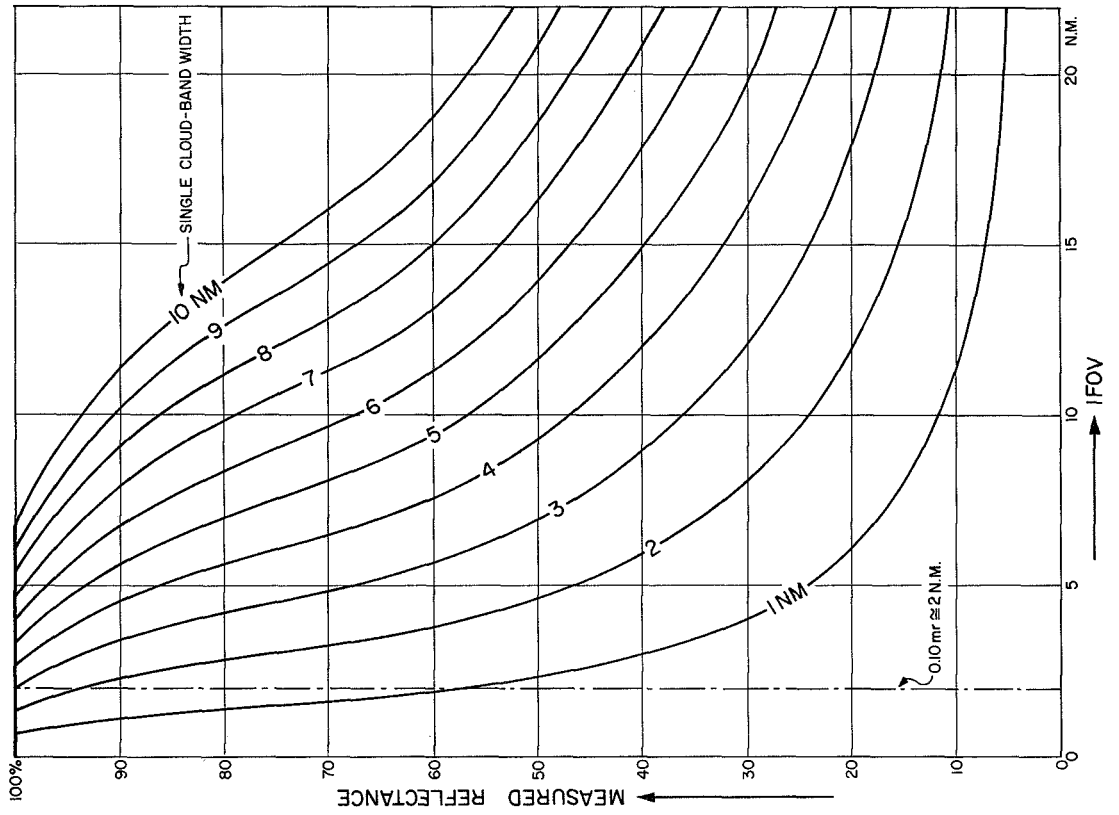

Fig. 12. Maximum measured reflectance obtainable from various IFOVs and widths (W) of single cloud bands of infinite length.

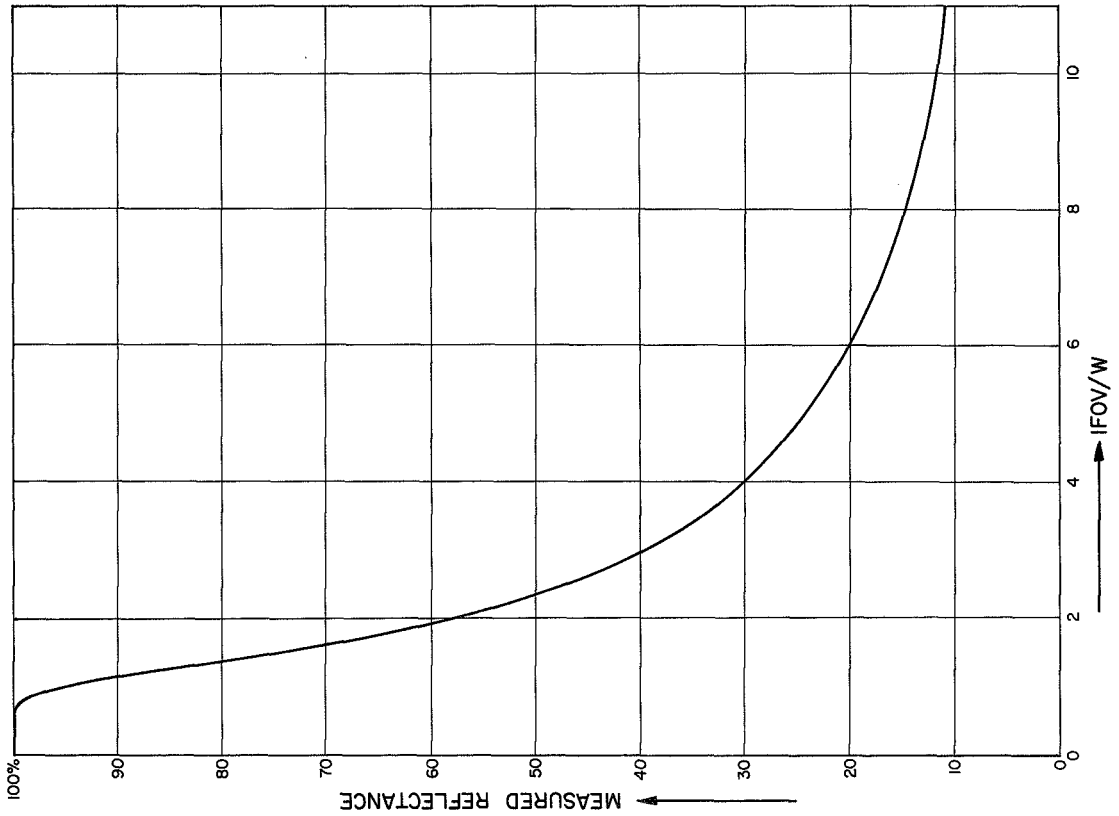

Fig. 11. Maximum measured reflectance obtainable from various IFOV/W for single cloud band of infinite length.

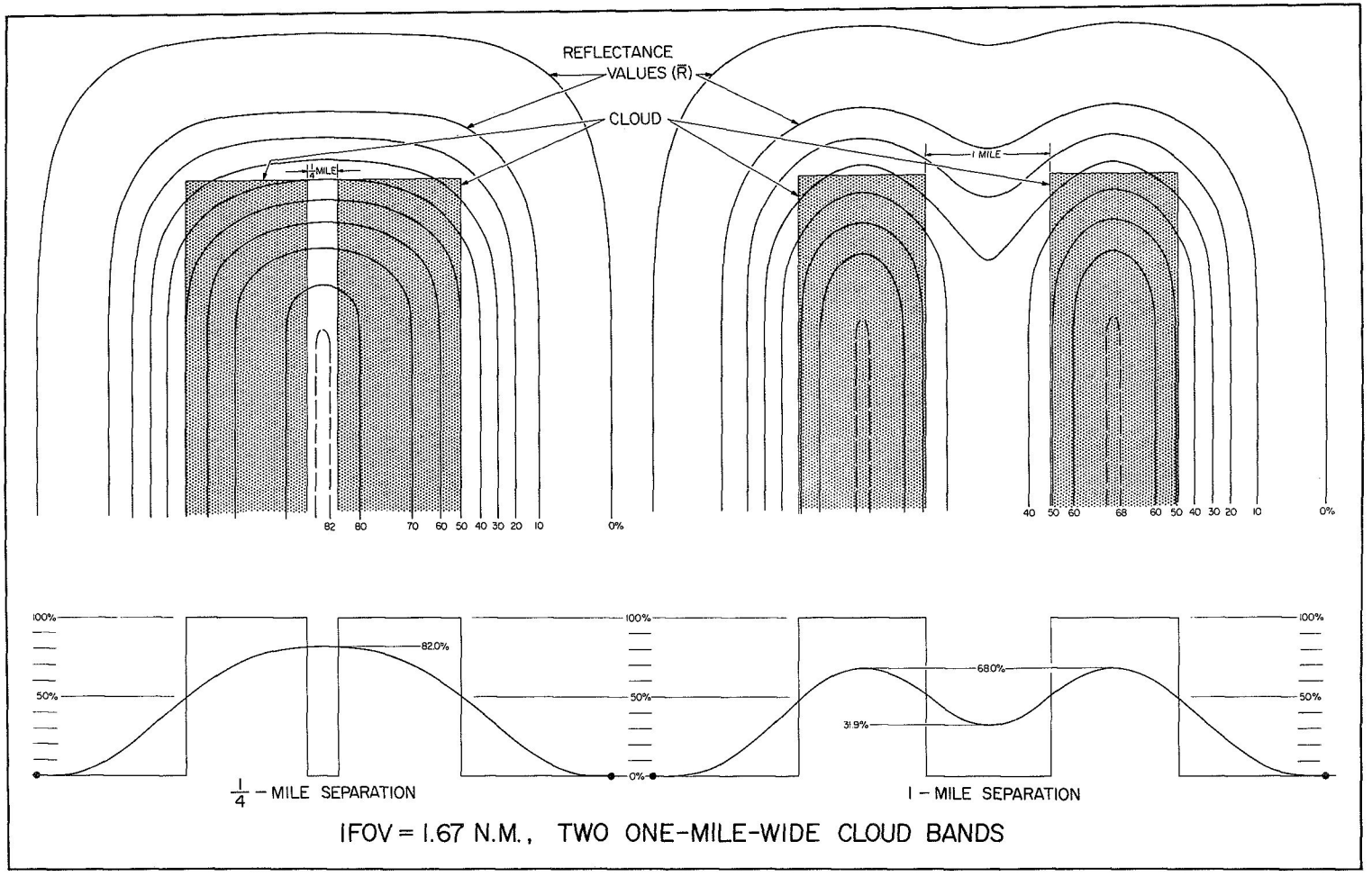

Fig. 13. Simulated patterns of relfectance values (upper portion) relative to various distances separating twin 1-mile wide cloud bands and corresponding profiles (lower portion) when scanned by a 1.67 n.m. IFOV radiometer. The stippled areas denote the twin 1-mile-wide cloud band. The curves in the lower portion represent computed reflectance while the vertical bar areas indicate response from theoretically zero IFOV.

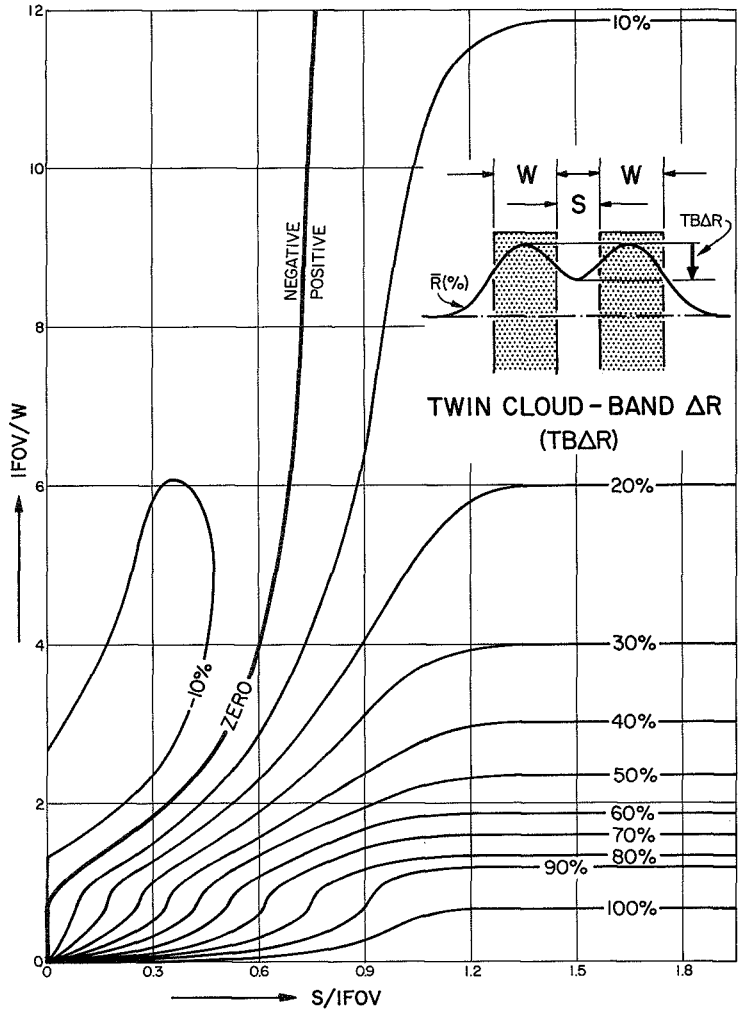

Fig. 14. Twin cloud band ΔR , TBΔR , relationship between the ratios S/IFOV and IFOV/W. Computed TBΔR does not exceed 100%. W is the uniform width of the twin cloud bands and S is the distance separating them.

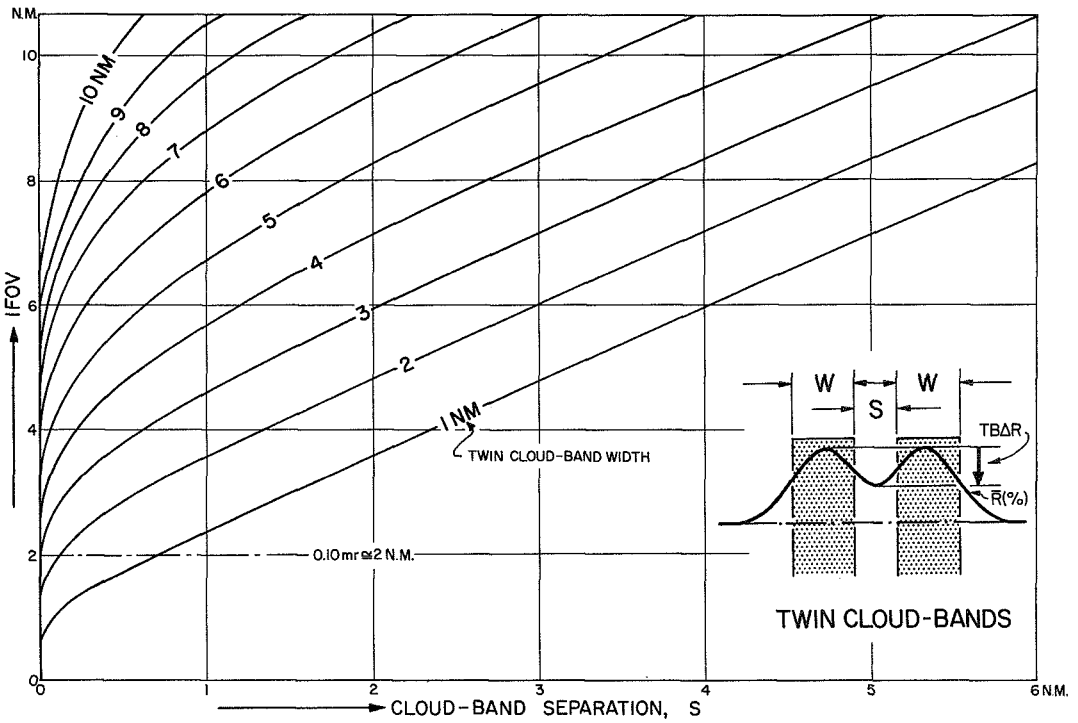

Fig. 15. Detection of separation between clouds in twin cloud bands of various widths as scanned by different IFOV through reflectance measurements.

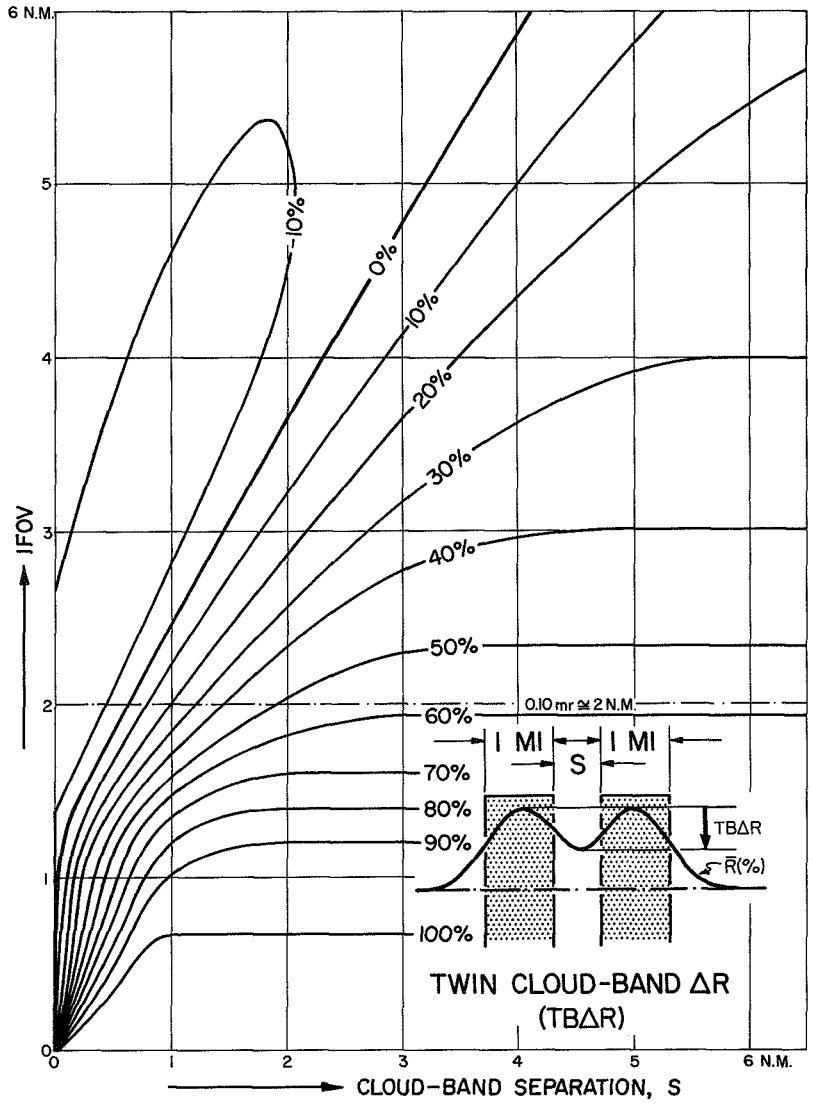

Fig. 16. Twin cloud band ΔR , $TB\Delta R$, for twin 1-mile-wide cloud bands as scanned by different IFOV. For any IFOV, individual clouds in the system become detectable at distances beyond the 0% line. No values exceed 100%.

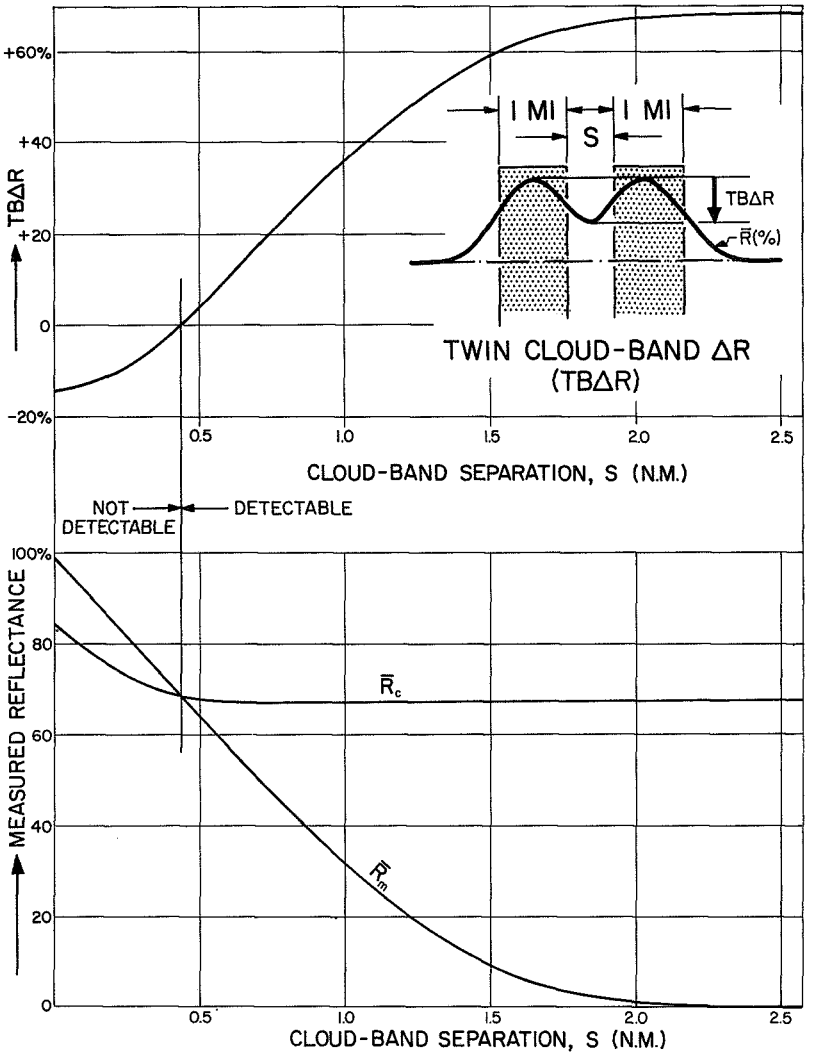

Fig. 17. Measured reflectance curves (lower portion) for cloud band centers, $\bar{R}_c$, and midpoint between them, $\bar{R}_m$, and corresponding $TB\Delta R$ (upper portion) for twin 1-mile-wide cloud bands of infinite length for IFOV = 1.67 n.m.

MESOMETEOROLOGY PROJECT - - - RESEARCH PAPERS

(Continued from front cover)

42.* A Study of Factors Contributing to Dissipation of Energy in a Developing Cumulonimbus - Rodger A. Brown and Tetsuya Fujita

43. A Program for Computer Gridding of Satellite Photographs for Mesoscale Research - William D. Bonner

44. Comparison of Grassland Surface Temperatures Measured by TIROS VII and Airborne Radiometers under Clear Sky and Cirriform Cloud Conditions - Ronald M. Reap

45. Death Valley Temperature Analysis Utilizing Nimbus I Infrared Data and Ground-Based Measurements - Ronald M. Reap and Tetsuya Fujita

46. On the "Thunderstorm-High Controversy" - Rodger A. Brown

47. Application of Precise Fujita Method on Nimbus I Photo Gridding - Lt. Cmd. Ruben Nasta

48. A Proposed Method of Estimating Cloud-top Temperature, Cloud Cover, and Emissivity and Whiteness of Clouds from Short- and Long-wave Radiation Data Obtained by TIROS Scanning Radiometers - T. Fujita and H. Grandoso

49. Aerial Survey of the Palm Sunday Tornadoes of April 11, 1965 - Tetsuya Fujita

50. Early Stage of Tornado Development as Revealed by Satellite Photographs - Tetsuya Fujita

51. Features and Motions of Radar Echoes on Palm Sunday, 1965 - D. L. Bradbury and T. Fujita

52. Stability and Differential Advection Associated with Tornado Development - Tetsuya Fujita and Dorothy L. Bradbury

53. Estimated Wind Speeds of the Palm Sunday Tornadoes - Tetsuya Fujita

54. On the Determination of Exchange Coefficients: Part II - Rotating and Nonrotating Convective Currents - Rodger A. Brown

55. Satellite Meteorological Study of Evaporation and Cloud Formation over the Western Pacific under the Influence of the Winter Monsoon - K. Tsuchiya and T. Fujita

56. A Proposed Mechanism of Snowstorm Mesojet over Japan under the Influence of the Winter Monsoon - T. Fujita and K. Tsuchiya

57. Some Effects of Lake Michigan upon Squall Lines and Summertime Convection - Walter A. Lyons

58. Angular Dependence of Reflection from Stratiform Clouds as Measured by TIROS IV Scanning Radiometers - A. Rabbe

59. Use of Wet-beam Doppler Winds in the Determination of the Vertical Velocity of Raindrops inside Hurricane Rainbands - T. Fujita, P. Black and A. Loesch

60. A Model of Typhoons Accompanied by Inner and Outer Rainbands - Tetsuya Fujita, Tatsuo Izawa,, Kazuo Watanabe and Ichiro Imai

61. Three-Dimensional Growth Characteristics of an Orographic Thunderstorm System - Rodger A. Brown

62. Split of a Thunderstorm into Anticyclonic and Cyclonic Storms and their Motion as Determined from Numerical Model Experiments - Tetsuya Fujita and Hector Grandoso

63. Preliminary Investigation of Peripheral Subsidence Associated with Hurricane Outflow - Ronald M. Reap

64. The Time Change of Cloud Features in Hurricane Anna, 1961, from the Easterly Wave Stage to Hurricane Dissipation - James E. Arnold

65. Easterly Wave Activity over Africa and in the Atlantic with a Note on the Intertropical Convergence Zone during Early July 1961 - James E. Arnold

66. Mesoscale Motions in Oceanic Stratus as Revealed by Satellite Data - Walter A. Lyons and Tetsuya Fujita

67. Mesoscale Aspects of Orographic Influences on Flow and Precipitation Patterns - Tetsuya Fujita

68. A Mesometeorological Study of a Subtropical Mesocyclone -Hidetoshi Arakawa, Kazuo Watanabe, Kiyoshi Tsuchiya and Tetsuya Fujita

69. Estimation of Tornado Wind Speed from Characteristic Ground Marks - Tetsuya Fujita, Dorothy L. Bradbury and Peter G. Black

70. Computation of Height and Velocity of Clouds from Dual, Whole-Sky, Time-Lapse Picture Sequences - Dorothy L. Bradbury and Tetsuya Fujita

71. A Study of Mesoscale Cloud Motions Computed from ATS-I and Terrestrial Photographs - Tetsuya Fujita, Dorothy L. Bradbury, Clifford Murino and Louis Hull

72. Aerial Measurement of Radiation Temperatures over Mt. Fuji and Tokyo Areas and Their Application to the Determination of Ground- and Water-Surface Temperatures - Tetsuya Fujita, Gisela Baralt and Kiyoshi Tsuchiya

73. Angular Dependence of Reflected Solar Radiation from Sahara Measured by TIROS VII in a Torquing Maneuver - Rene Mendez.

74. The Control of Summertime Cumuli and Thunderstorms by Lake Michigan During Non-Lake Breeze Conditions - Walter A. Lyons and John W. Wilson

75. Heavy Snow in the Chicago Area as Revealed by Satellite Pictures - James Bunting and Donna Lamb

76. A Model of Typhoons with Outflow and Subsidence Layers - Tatsuo Izawa

* out of print

(continued on outside back cover)

SATELLITE AND MESOMETEOROLOGY RESEARCH PROJECT - - - PAPERS

(Continued from inside back cover)

77. Yaw Corrections for Accurate Gridding of Nimbus HRIR Data - Roland A. Madden

78. Formation and Structure of Equatorial Anticyclones Caused by Large-Scale Cross Equatorial Flows Determined by ATS I Photographs - Tetsuya T. Fujita and Kazuo Watanabe and Tatsuo Izawa

79. Determination of Mass Outflow from a Thunderstorm Complex Using ATS III Pictures - T. T. Fujita and D. L. Bradbury

80. Development of a Dry Line as Shown by ATS Cloud Photography and Verified by Radar and Conventional Aerological Data - Dorothy L. Bradbury

81. Dynamical Analysis of Outflow from Tornado-Producing Thunderstorms as Revealed by ATS III Pictures - K. Ninomiya

82. Computation of Cloud Heights From Shadow Positions through Single Image Photogrammetry of Apollo Pictures - T. T. Fujita

83. Aircraft, Spacecraft, Satellite and Radar Observations of Hurricane Gladys, 1968 - R. Cecil Gentry, Tetsuya T. Fujita and Robert C. Sheets

84. Basic Problems on Cloud Identification Related to the Design of SMS-GOES Spin Scan Radiometers - Tetsuya Theodore Fujita

85. Mesoscale Modification of Synoptic Situations over the Area of Thunderstorms' Development as Revealed by ATS III and Aerological Data - K. Ninomiya

86. Palm Sunday Tornadoes of April 11, 1965 - T. T. Fujita, Dorothy L. Bradbury, and C. F. Van Thullenar. (Reprint from Mon. Wea. Rev., 98, 29-69, 1970)